Supplementary Information: Steric scattering of rod-like swimmers in low Reynolds number environments

Kentaro Hoeger and Tristan Ursell
Department of Physics, University of Oregon
Eugene, OR 97424

1 Model of Steric Scattering

Herein we develop a steric model of a rod-like swimmer (e.g. bacterium) that aligns with a surface and subsequently scatters from it. Based on observed data, these geometric relationships are sufficient to describe the interaction and the resulting relationship between cellular motion with respect to an oriented surface, specifically predicting the relationship between the impact parameter b and the mean scattering angle $\langle\theta\rangle$, as well as the duration of interaction (at constant swimming speed) and the angle of exit, β. Please see the main text for model assumptions.

1.1 Geometric Constraints

As a matter of temporary convenience, we assume that the red point in Fig. 1 is the origin of a Cartesian coordinate system. The motion of each of the points P_1 and P_2 are parametrically described by $(x_1(t), y_1(t))$ and $(x_2(t), y_2(t))$, respectively, thus all possible dynamics are captured by these four dependent variables. First, note that we are treating the cell as a line-object propelled on-axis from the rear. We assume that the length of the cell L does not change, mandating that

$$(x_2 - x_1)^2 + (y_2 - y_1)^2 = L^2 \tag{1}$$

and we assume (for now) that the point of contact P_2 is always in contact, sliding along the surface, until such time as the bacterium leaves the surface, hence

$$y_2 = x_2 \tan(\theta). \tag{2}$$

The length L is the distance between the leading tip of the cell and the effective point of propulsion, a little longer than the cell body, we use $L = 3.75\,\mu m$ throughout this work.

1.2 Drag-limited Dynamics

We first build up a simpler model of a swimming cell scattering from a flat surface oriented by an angle θ with respect to the horizontal (see Fig. 1), and then extend this model to account for movement along a curved (in this case circular) surface of radius R.

Swimming bacteria exist at low Reynolds number ($\sim 10^{-5} - 10^{-4}$) where viscous drag limits movement of the points P_1 and P_2, and hence the velocities of points P_1 and P_2 are proportional to the net force on those points with a fixed mobility σ for each point. The propulsion force F, independent of any state of motion can be decomposed into a component that is parallel to the scattering surface $F_{\parallel}$ and a component normal to the surface $F_{\perp}$, such that given the current angle α,

$$F_{\perp} = F \sin(\alpha) \tag{3}$$

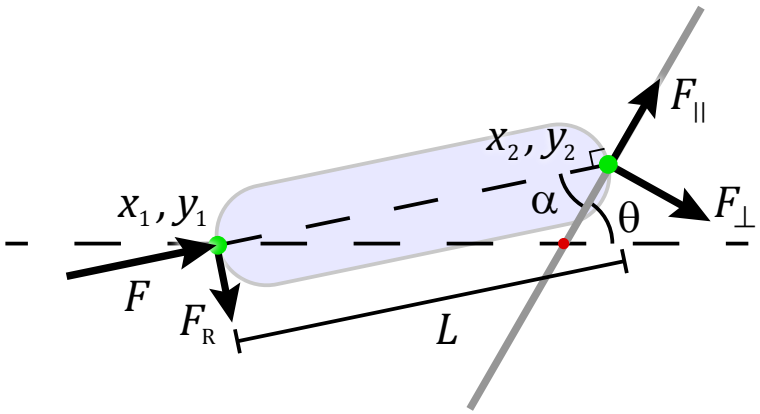

Figure 1: Relationships between bacterial orientation (α), surface orientation (θ), cell length (L), and propulsion force (F), for a cell orienting to a flat inclined surface. Note that for visual clarity, we draw the cell as a rod-shaped pusher without flagella and not to accurate proportions.

and

$$F_{\|} = F\cos(\alpha). \tag{4}$$

We approach the equations of motion as a problem of finding (x_i, y_i) as functions of $\alpha(t)$ and its derivatives. The force parallel to the surface translates the point P_2 according to

$$\dot{x}_2 = F\sigma\cos(\alpha)\cos(\theta) \tag{5}$$

$$\dot{y}_2 = F\sigma\cos(\alpha)\sin(\theta) \tag{6}$$

The distance $x_2 - x_1$ is also defined geometrically by

$$x_2 - x_1 = L\cos(\theta - \alpha) \tag{7}$$

and hence its time derivative is

$$\dot{x}_2 - \dot{x}_1 = \dot{\alpha}L\sin(\theta - \alpha) \tag{8}$$

such that

$$\dot{x}_1 = \dot{x}_2 - \dot{\alpha}L\sin(\theta - \alpha) = F\sigma\cos(\alpha)\cos(\theta) - \dot{\alpha}L\sin(\theta - \alpha) \tag{9}$$

Looking back at the constraint for L and taking the time derivative

$$(x_2 - x_1)^2 + (y_2 - y_1)^2 = L^2 \;\rightarrow\; (x_2 - x_1)(\dot{x}_2 - \dot{x}_1) + (y_2 - y_1)(\dot{y}_2 - \dot{y}_1) = 0 \tag{10}$$

Then using our results above

$$\dot{\alpha}L\sin(\theta - \alpha) + \frac{y_2 - y_1}{x_2 - x_1}(\dot{y}_2 - \dot{y}_1) = 0 \tag{11}$$

and with

$$\frac{y_2 - y_1}{x_2 - x_1} = \tan(\theta - \alpha) \tag{12}$$

this simplifies to

$$\dot{\alpha}L\cos(\theta - \alpha) + \dot{y}_2 - \dot{y}_1 = 0 \;\rightarrow\; \dot{y}_1 = \dot{y}_2 + \dot{\alpha}L\cos(\theta - \alpha) \tag{13}$$

and finally

$$\dot{y}_1 = F\sigma\cos(\alpha)\sin(\theta) + \dot{\alpha}L\cos(\theta - \alpha) \tag{14}$$

Then the projection of the perpendicular force $F_\perp$ onto the coordinate perpendicular to the axis of the cell is what causes the cell body to rotate with respect to the surface, and thus

$$F_R = F_\perp \sin\left(\frac{\pi}{2} - \alpha\right) = F \sin(\alpha)\cos(\alpha) \tag{15}$$

Finally, rotation of the cell is

$$\dot{\alpha} = \frac{F_R \sigma}{L} = -\frac{F\sigma}{L}\sin(\alpha)\cos(\alpha). \tag{16}$$

We note that the natural length scale is L (as it has nothing to do with R) and the natural time scale is $L/F\sigma$, such that the equations of motion can be non-dimensionalized and written

$$\dot{\alpha} = -\sin(\alpha)\cos(\alpha) \tag{17}$$

and then

$$\dot{x}_2 = \cos(\alpha)\cos(\theta) \tag{18}$$

$$\dot{y}_2 = \cos(\alpha)\sin(\theta) \tag{19}$$

$$\dot{x}_1 = \cos(\alpha)\cos(\theta) - \dot{\alpha}\sin(\theta - \alpha) \tag{20}$$

$$\dot{y}_1 = \cos(\alpha)\sin(\theta) + \dot{\alpha}\cos(\theta - \alpha) \tag{21}$$

Finally, the differential equation for α with initial condition $\alpha(0) = \alpha_o$ is solved by

$$\alpha(t) = -\frac{1}{2}\tan^{-1}\left[\frac{2e^{-t}\tan(\alpha_o)}{1 + (e^{-t}\tan(\alpha_o))^2}\ ,\ \frac{1 - (e^{-t}\tan(\alpha_o))^2}{1 + (e^{-t}\tan(\alpha_o))^2}\right] \tag{22}$$

where the effect of the initial condition is to shift the time axis by $t_o = -\ln(\tan(\alpha_o))$. For long times or small α_o this can be approximated simply as

$$\alpha(t) \simeq \alpha_o e^{-t}. \tag{23}$$

This was the case for a rod-like object orienting to a flat surface tilted by an angle θ.

1.3 Contact Friction

To determine the potential role of friction, we note that if the parallel force exceeds the friction force then the point of contact will move, this can be stated as

$$F_\parallel \geq \mu F_\perp \tag{24}$$

where μ is the frictional coefficient. This leads to a critical impact angle

$$\alpha_c = \tan^{-1}\left(\frac{1}{\mu}\right). \tag{25}$$

This is a condition for the balance between frictional and sliding forces – our data frequently show cells impacting the steric object essentially head-on, with subsequent sliding along the surface, indicating that the friction $\mu \ll 1$, supporting the model assumption that the motion is drag-limited.

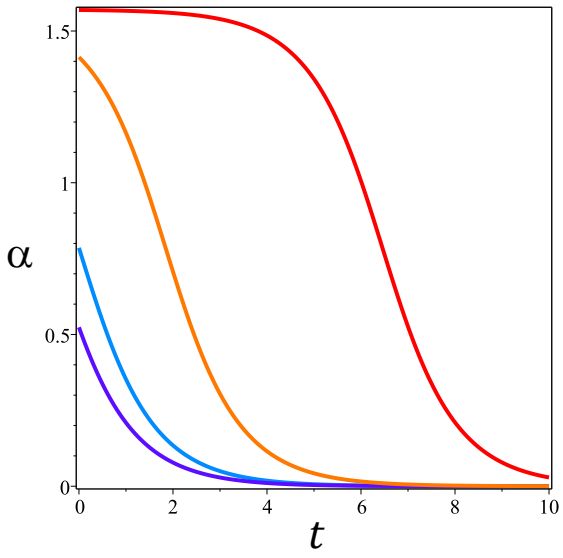

Figure 2: Bacterial orientation (α) with respect to a flat inclined surface as a function of time (t) in dimensionless units for (left to right) $\alpha_o = \pi/6, \pi/4, 0.9\pi/2, 0.999\pi/2$.

1.4 Interactions with a Curved Surface

Assuming that viscous drag is the primary constraint on motion, we assume that all velocities are proportional to net force with a fixed mobility σ. The propulsion force F, independent of any state of motion can be decomposed into a component that is parallel to the scattering surface $F_\parallel$ and a component normal to the surface $F_\perp$, such that given the current angle α,

$$F_\perp = F\sin(\alpha) \tag{26}$$

and

$$F_\parallel = F\cos(\alpha). \tag{27}$$

For simplicity we assume that the circle's center is the coordinate origin, and hence

$$x_2 = -R\cos(\phi) \tag{28}$$

$$y_2 = R\sin(\phi) \tag{29}$$

and thus

$$\dot{x}_2 = \dot{\phi}R\sin(\phi) \tag{30}$$

$$\dot{y}_2 = \dot{\phi}R\cos(\phi) \tag{31}$$

Using the parallel force we can also write

$$\dot{y}_2 = F_\parallel\sigma\cos(\phi) = F\sigma\cos(\alpha)\cos(\phi) \tag{32}$$

$$\dot{x}_2 = F_\parallel\sigma\sin(\phi) = F\sigma\cos(\alpha)\sin(\phi) \tag{33}$$

Both of these equations dictate that

$$\dot{\phi} = \frac{F\sigma}{R}\cos(\alpha) \tag{34}$$

which, using the natural length scale L and natural time scale $L/F\sigma$, gives

$$\dot{\phi} = \rho\cos(\alpha) \tag{35}$$

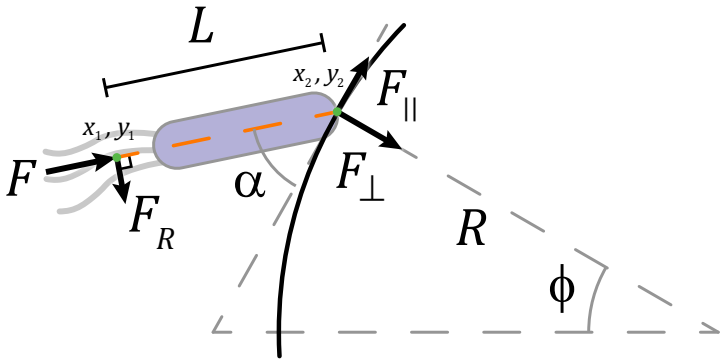

Figure 3: Relationships between the various forces and geometrical parameters of the circular model, including bacterial orientation (α), surface orientation (ϕ), cell length (L), and propulsion force (F).

with $\rho = L/R$, and the initial condition is related to the impact parameter by

$$\phi_o = \sin^{-1}\left(\frac{b}{R}\right) \tag{36}$$

and likewise the initial value of α is

$$\alpha_o = \frac{\pi}{2} - \phi_o \tag{37}$$

because we assume the cell impacts in a flat orientation (i.e. $y_1 = y_2$). Then the rate change of α due to *torque* is

$$\dot{\alpha}_T = -\frac{F_R \sigma}{L} \tag{38}$$

where

$$F_R = F_\perp \sin\left(\frac{\pi}{2} - \alpha\right) = F_\perp \cos(\alpha) = F\cos(\alpha)\sin(\alpha) \tag{39}$$

and the rate change of α due to the *surface curvature* is

$$\dot{\alpha}_C = -\dot{\phi} \tag{40}$$

then

$$\dot{\alpha} = \dot{\alpha}_T + \dot{\alpha}_C = \frac{F\sigma}{L}\cos(\alpha)\sin(\alpha) - \frac{F\sigma}{R}\cos(\alpha) \tag{41}$$

and upon non-dimensionalization

$$\dot{\alpha} = -\cos(\alpha)\sin(\alpha) - \rho\cos(\alpha) = -\cos(\alpha)\left(\sin(\alpha) + \rho\right) \tag{42}$$

This model predicts that if the cell is perpendicular to the surface ($\alpha = \pi/2$) then $\dot{\alpha} = 0$, same as the flat surface. However, it also predicts that there is a non-zero critical angle

$$\alpha_c = -\sin^{-1}(\rho) \;\rightarrow\; \rho < 1 \tag{43}$$

that results in a stable orientation with respect to the surface, however, the fact that that angle is negative means that this only occurs for cells on the 'inside' (i.e. negative curvature), which may be part of the consistent orientation of motile *Bacillus subtilis* cells observed on the *inside* curvature of a circular hole[1].

[1]E. Lushi, H. Wioland, R.E. Goldstein; Fluid flows created by swimming bacteria drive self-organization in confined suspensions (2014). *PNAS* **111**, 9733 - 9738.

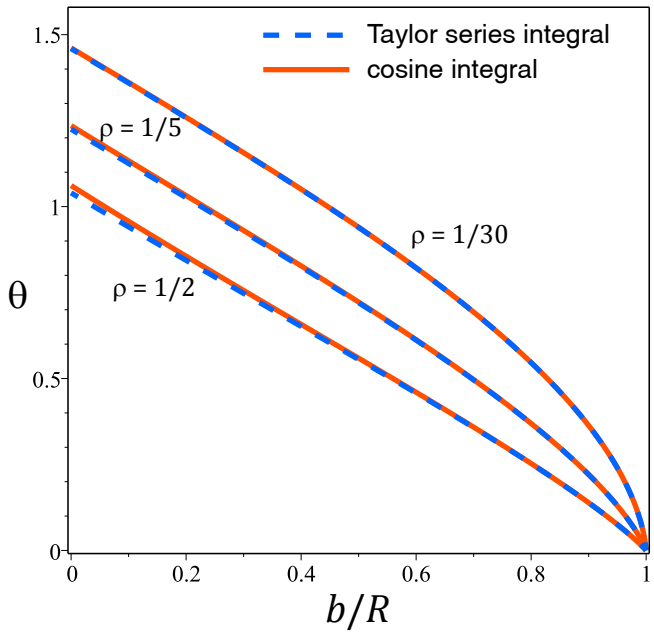

Figure 4: Relationship between impact parameter b/R and the output angle θ for values of ρ indicated.

For the moment let us make analytic headway by assuming small α_o, and thus the differential equation becomes

$$\dot{\alpha} \simeq -\alpha - \rho \;\rightarrow\; \alpha = e^{-t}\left(\alpha_o + \rho\right) - \rho, \tag{44}$$

noting that the flat surface case (earlier) corresponds to $\rho \to 0$. The assumption of the model is that the bacterium leaves the surface when $\alpha = 0$, thus the time when that happens is

$$t_c = \ln\left(\frac{\alpha_o}{\rho} + 1\right) \tag{45}$$

and the angle ϕ at which it leaves is determined by

$$\dot{\phi} = \rho\cos(\alpha) \;\rightarrow\; \phi_c = C + \rho\int_0^{t_c}\cos(\alpha)\mathrm{d}t \simeq C + \rho\int_0^{t_c}\left[1 - \frac{\alpha^2}{2}\right]\mathrm{d}t \tag{46}$$

where C is a constant such that $\phi(0) = \phi_o$. Even using the linearized model to determine $\alpha(t)$, this integral has a complicated solution, however approximating cosine by its first two Taylor series terms we can find

$$\phi_c = \frac{\pi}{2} - \rho\frac{\alpha_o^2}{4} + \alpha_o\left(1 - \frac{\rho}{\alpha_o}\ln\left(\frac{\alpha_o}{\rho} + 1\right)\right)\left(\frac{\rho^2}{2} - 1\right) \tag{47}$$

Then finally, the measured exit angle is given by

$$\theta = \frac{\pi}{2} - \phi_c = \rho\frac{\alpha_o^2}{4} - \alpha_o\left(1 - \frac{\rho}{\alpha_o}\ln\left(\frac{\alpha_o}{\rho} + 1\right)\right)\left(\frac{\rho^2}{2} - 1\right) \tag{48}$$

with $\alpha_o = \cos^{-1}\left(\frac{b}{R}\right)$. Similarly, the limit when $\rho \to 0$ gives the initial condition $\theta = \alpha_o$, consistent with the flat-surface model. The models overlaid with data in the main text and SI were calculated using this differential equation, but were solved exactly (numerically) (as opposed to applying the small α_o approximation).

1.5 Interaction Time

An interaction with a pillar of radius R was computationally triggered when a bacterium came within $R+\delta$ of the pillar center, where $\delta = 2.2\,\mu m$ is the radial zone around the pillar inside of which we measured interactions. Thus for a given value of b, the initial straight line path from entry into the interaction zone until contact with the pillar has a length

$$s_1 = R\left[\sqrt{\left(1+\frac{\delta}{R}\right)^2 - \left(\frac{b}{R}\right)^2} - \sqrt{1-\left(\frac{b}{R}\right)^2}\right] \tag{49}$$

and applying the average swim speed $\langle v\rangle$, a transit time of

$$t_1 = \frac{s_1}{\langle v\rangle}. \tag{50}$$

Likewise, after the cell has slide around the pillar and rotated to be tangent with the pillar surface, the length from that point to exit of the interaction zone is

$$s_3 = R\sqrt{\left(1+\frac{\delta}{R}\right)^2 - 1} \tag{51}$$

and a transit time of

$$t_3 = \frac{s_3}{\langle v\rangle} \tag{52}$$

The time spent sliding and rotating around the pillar can be found exactly from the differential equation

$$\dot{\alpha} = -\cos(\alpha)(\sin(\alpha)+\rho) \tag{53}$$

which can be integrated directly for the time at which certain values of α are achieved

$$t + C = -\int \frac{\mathrm{d}\alpha}{\cos(\alpha)(\sin(\alpha)+\rho)} = \frac{\ln(\sin(\alpha)+1)}{2-2\rho} + \frac{\ln(\sin(\alpha)-1)}{2+2\rho} + \frac{\ln(\sin(\alpha)+\rho)}{(\rho+1)(\rho-1)} \tag{54}$$

where C is an unimportant constant. The time between contact and tangency is given by

$$t_2 = \frac{L}{\langle v\rangle}\left[t|_{\alpha=0} - t|_{\alpha=\alpha_o}\right] \tag{55}$$

where we have now accounted for the natural timescale, and this simplifies to

$$t_2 = -\frac{L}{\langle v\rangle}\left[\frac{\ln(\sin(\alpha_o)+1)}{2(1-\rho)} + \frac{\ln\left(|\sin(\alpha_o)-1|\right)}{2(1+\rho)} + \frac{\ln\left(\frac{\sin(\alpha_o)}{\rho}+1\right)}{(\rho-1)(\rho+1)}\right] \tag{56}$$

Then the total interaction time is

$$t_{\text{int}} = t_1 + t_2 + t_3 = t_f - t_i. \tag{57}$$

In our data processing, we subtracted a constant length (of $1\,\mu m$) from s_1 to account for the offset between the position of the tip which makes contact with the pillar and the position of the cell centroid from image processing, that offset is applied consistently to all data processing and figures.

SI Figure 7, shows the measured data overlaid with the model predictions. There is a notable degradation of signal for increasing R due to two distinct effects. First, as discussed in sect. 6 below, the rate at which data can be collected (and hence to total amount of data collected) decreases rapidly with increasing R. Second, we employed the average speed in our model to set the natural time scale which relates linearly to the interaction time. All else being equal, populations of cells exhibit a distribution of speeds, and thus we expect a distribution of interaction times. Indeed, at least some part of the variance in interaction times is due to variations in the swim speed of individual cells. Larger pillars have longer interactions times, and thus variability in interaction times due to speed increases with pillar radius.

2 Predictions for Control Data

As a test for our entire image analysis and data pipeline, we imaged cells swimming through open regions of our device, that is, devoid of any steric obstruction except the upper and lower surfaces. We created fictitious interaction by zones by defining a typical (fictitious) pillar dimension ($R = 5.8\,\mu m$) and corresponding interaction zone of width $\delta = 2.2\,\mu m$. As bacteria swam through the interaction zone, we processed their trajectories in precisely the same way as we processed actual steric interactions. We constructed the same plots of: dimensionless impact parameter (b/R) vs. scattering angle (θ), b/R vs. exit angle (ϕ), and b/R vs. interaction time, and we calculated the expected mean values of those relationships. The calculations below assume that the persistence length of the isotropic persistent random walk of the cellular trajectories is much longer than $R + \delta$.

In particular, if diffusion of a trajectory across the interaction zone was isotropic, then the entry angle (of 0) should, on average, be zero upon exit, regardless of b and hence

$$\langle\theta\rangle\,(\tfrac{b}{R}) = 0. \tag{58}$$

Similarly, if diffusion is isotropic the point of entry into the interaction zone, specified by b, has the same mean y-axis ($y = b$) value at the point of exit, giving the exit angle of

$$\langle\beta\rangle = \sin^{-1}\left(\frac{b/R}{1+\frac{\delta}{R}}\right) \tag{59}$$

Finally, the interaction time, that is, the time from entry to exit, will be dominated by approximately straight trajectories that exit, on average, at the same $y = b$ value at both points. The time to execute that trajectory is

$$t_{\text{int}} = 2\frac{R}{\langle v\rangle}\sqrt{\left(1+\frac{\delta}{R}\right)^2 - \left(\frac{b}{R}\right)^2}. \tag{60}$$

The data and overlaid control models are shown in Fig. 14.

3 Measured Chiral Symmetry

Given the mid-plane reflection symmetry of the device (in Z) we expected the CW- and CCW-rotator distributions (including counter-rotators) to be approximately symmetric when mirrored across the $b = 0$ and $\theta = 0$ lines. We tested this by applying the appropriate symmetry operations to the data and then compared the mean scattering angles of each lobe for $0 \leq |b/R| \leq 1$. For each pillar radius the mean scattering angles between the two lobes were symmetric, modulo point-to-point variations. As pillar radius increased, there was a small chiral asymmetry between the two lobes (SI Fig. 15). Through initial, iterative improvement of the fabrication process we observed that decreasing the systematic tapering of pillars – resulting from photolithography – reduced these chiral asymmetries. Thus the observed asymmetry likely arises from small, systematic pillar tapering ($\leq 4\%$) that asymmetrically affects chiral coupling at the upper and lower surfaces where the difference in pillar radius is greatest.

4 MLE Fitting

In order to extract parameters that both describe the trends of the scattering process and to compare with the predictions of our model, we applied Maximum-likelihood estimation to determine parameter values and 95% confidence intervals. For each bin in b, we started with a von Mises distribution modified to include a constant offset that accounts for the uniform scattering angle that corresponds to non-directional

'tumble-collisions' in our measured data

$$\rho(\theta;\langle\theta\rangle,\sigma,c)=\frac{c}{1+2\pi c}\left(1+\frac{e^{\frac{\cos(\theta-\langle\theta\rangle)}{\sigma^2}}}{2\pi c I_0(\sigma^{-2})}\right) \tag{61}$$

where θ is the measured scattering angle, σ is the width of the distribution in radians (analogous to the standard deviation of a Gaussian), $\langle\theta\rangle$ is the mean scattering angle, c is the offset parameter, and I_0 is the modified Bessel function of the first kind. The log-likelihood function is then

$$\ln(\mathcal{L}(\langle\theta\rangle,\sigma,c))=\sum_{i=1}^{N}\ln(\rho(\theta_i;\langle\theta\rangle,\sigma,c)) \tag{62}$$

where the index i spans the measured values of θ. This simplifies to

$$\ln(\mathcal{L})=N\ln\left(\frac{c}{1+2\pi c}\right)+\sum_{i=1}^{N}\ln\left(1+\frac{e^{\frac{\cos(\theta_i-\langle\theta\rangle)}{\sigma^2}}}{2\pi c I_0(\sigma^{-2})}\right) \tag{63}$$

where N is the total number of data points and the fraction of tumble-collisions is

$$f_{\text{tumb}}=\frac{2\pi c}{1+2\pi c} \tag{64}$$

We numerically sampled the log-likelihood function over reasonable ranges of all three parameters, and found the mode values for the parameters with 95% confidence intervals specified from the respective marginal distributions. An example of this data processing routine is shown SI Fig. 9.

5 Device Fabrication

Bacterial scattering events were measured in atypical microfluidic devices composed of a silicon wafer patterned with photoresist, and mechanically compressed against a thin layer of PDMS that was bonded to a glass slide. The top of the device consisted of a $5\,cm$ silicon wafer (University Wafer) onto which we spun a $0.5\,\mu m$ base layer of SU-8 2000.5 negative photoresist (Kayaku Advanced Materials Inc.). That layer was first soft baked at $95\,C$ for 1 minute, exposed at an energy density of $60\,mJ/cm^2$, and baked at $95\,C$ for another minute to cure the layer. This base layer increases adhesion of the pillars to the surface and improves feature resolution. Onto this existing layer of cured photoresist, we spun a $\sim 15\,\mu m$ layer of SU-8 2015 negative photoresist, and then soft baked it at $95\,C$ for three minutes. This thicker layer of photoresist was exposed with a quartz chromium mask containing the flow layout and pillared regions within the device, using a Suss MJB4 mask aligner. 'T-topping' (i.e. pillar taper) was minimized by filtering wavelengths below $360\,nm$ using a Hoya L-37 longpass filter (Hoya Optics Inc.) with an exposure energy density of $240\,mJ/cm^2$. The photoresist was developed by mildly agitating the silicon wafer in SU-8 developer for 3 minutes and then performing a final 'hard bake' for 10 minutes at $200\,C$ to increase structural stability.

The bottom piece consists of a thin layer of PDMS bonded to a glass slide that has inlet and outlet ports pre-drilled. Uncured PDMS is compressed between the pre-drilled slide and a second glass slide treated with tichlorosilane to minimize adhesion of the PDMS to this second slide. Small adhesive spacers between the two slides fixed the PDMS layer thickness to be $\sim 100\,\mu m$. The PDMS was bonded to the drilled slide by baking at $100\,C$ for 90 mins. Excess PDMS was removed from the inlet and outlet ports using a 1 mm biopsy punch. The patterned silicon wafer was then aligned to the inlet and outlet ports and mechanically compressed to create an airtight seal suitable for pulling suspensions of cells through the device with a syringe. Once filled with the cellular suspension, the device ports were sealed to halt any global flow, and the device was viewed from the bottom through the glass slide on an inverted microscope.

6 Estimating Basal Scattering Rates

In order to collect a large number of scattering events (∼30,000 to 100,000) per pillar radius, we used a low magnification objective (20x) that permitted viewing over a relatively large area (as compared to 40x or higher objectives). Given a mean cell density ρ_{cell} (number/area) and assuming that cells move independently and occupy the device isotropically, then there is some probability that the interaction zone of any single pillar is occupied by one and only one cell at a specific moment in time, given by the Poisson probability

$$p_1 = \lambda e^{-\lambda} \tag{65}$$

where

$$\lambda = \pi((R+\delta)^2 - R^2)\rho_{\text{cell}} \simeq 2\pi\delta R\rho_{\text{cell}} \tag{66}$$

is the expected number of cells in the interaction zone of any single pillar. The rate of observable scattering events that additionally meet the 'one-cell-per-interaction' filter, k_{scat}, is then

$$k_{\text{scat}} \propto Np_1 \tag{67}$$

where N is the number of pillars in a field-of-view, and $N \propto R^{-2}$. Thus, to leading order

$$k_{\text{scat}} \propto \frac{\delta\rho_{\text{cell}}}{R} e^{-2\pi\delta\rho_{\text{cell}}R}. \tag{68}$$

This demonstrates two points: (i) there is likely an optimal cell density for maximizing the rate of single-celled scattering events (we did not systematically explore this) and (ii) as R increases the observable scattering rate rapidly and monotonically decreases for a fixed field-of-view (i.e. constant magnification). This reduction in observable scattering rate with R is why there is less data (and hence higher relative variation) in the scattering maps for larger R. Finally, a valid scattering trajectory has only a single cell in the interaction *for the duration* of the interaction, and the interaction time (duration) increases with R. Thus k_{scat}, as stated in eqn. 68, is likely an upper bound with respect to R.

7 Supporting Figures

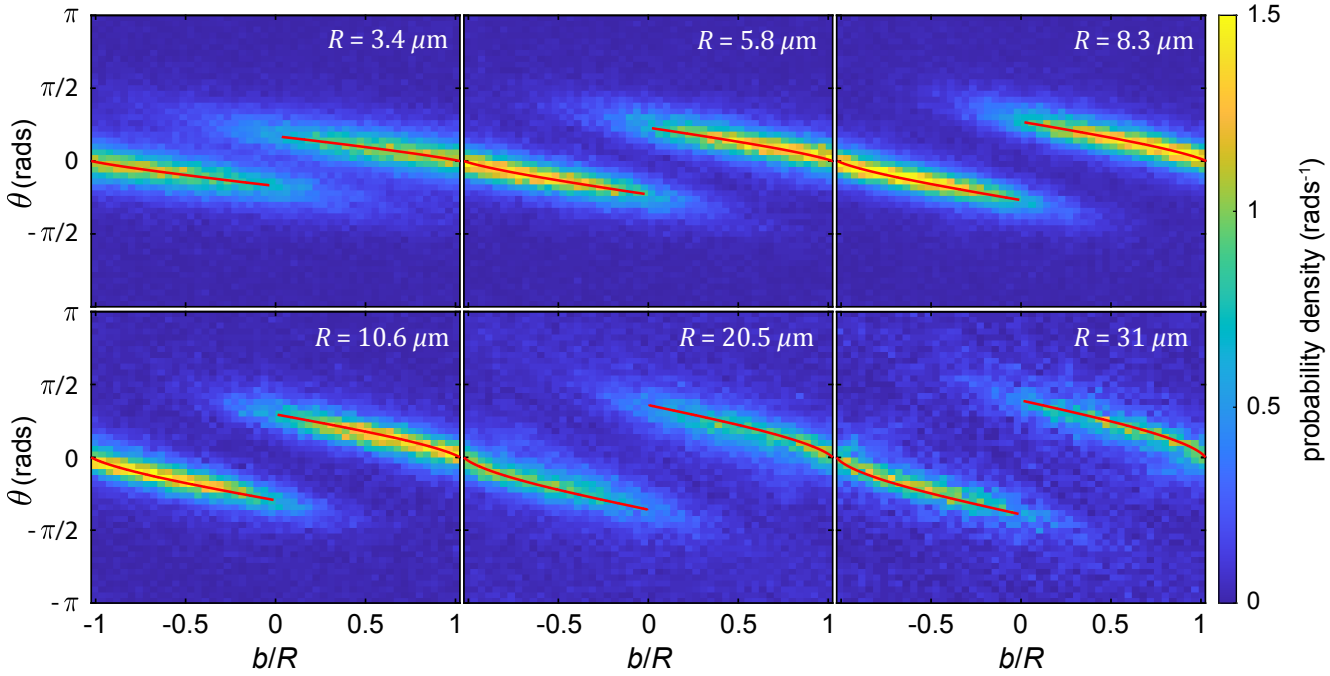

Figure 5: Scattering angle distributions as a function of dimensionless impact parameter b/R (same type of data as shown in Fig. 3C) across a range of pillar radii. The red lines show the model predictions for $\langle\theta\rangle$ given the listed radii. All calculations use the same exogenously specified cell length of $L = 3.75\,\mu m$. Notably, the 'signal-to-noise' ratio of measured data decreases with increasing pillar radius because the number of pillars and hence number of interactions we can observe in a single field-of-view decreases rapidly with R (see section 6).

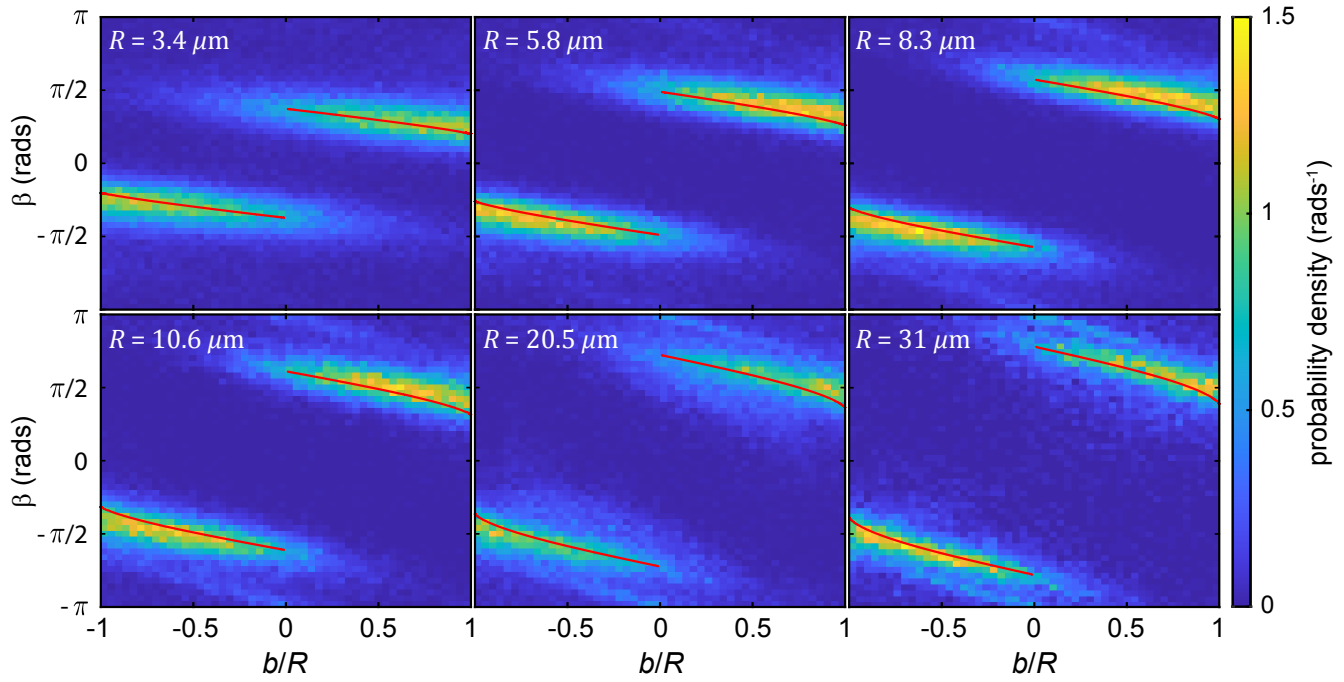

Figure 6: Interaction zone exit angle distributions (β) as a function of dimensionless impact parameter b/R, across a range of pillar radii (same type of data as Fig. 3D). The red lines show the model predictions for $\langle\beta\rangle$ given the listed radii. Model predictions were calculated by using the first cell trajectory point (in the rotated frame) outside of the interaction radius upon exit. All calculations use the same exogenously specified cell length of $L = 3.75\,\mu m$. Notably, the 'signal-to-noise' ratio of measured data decreases with increasing pillar radius because the number of pillars and hence number of interactions we can observe in a single field-of-view decreases rapidly with R (see section 6).

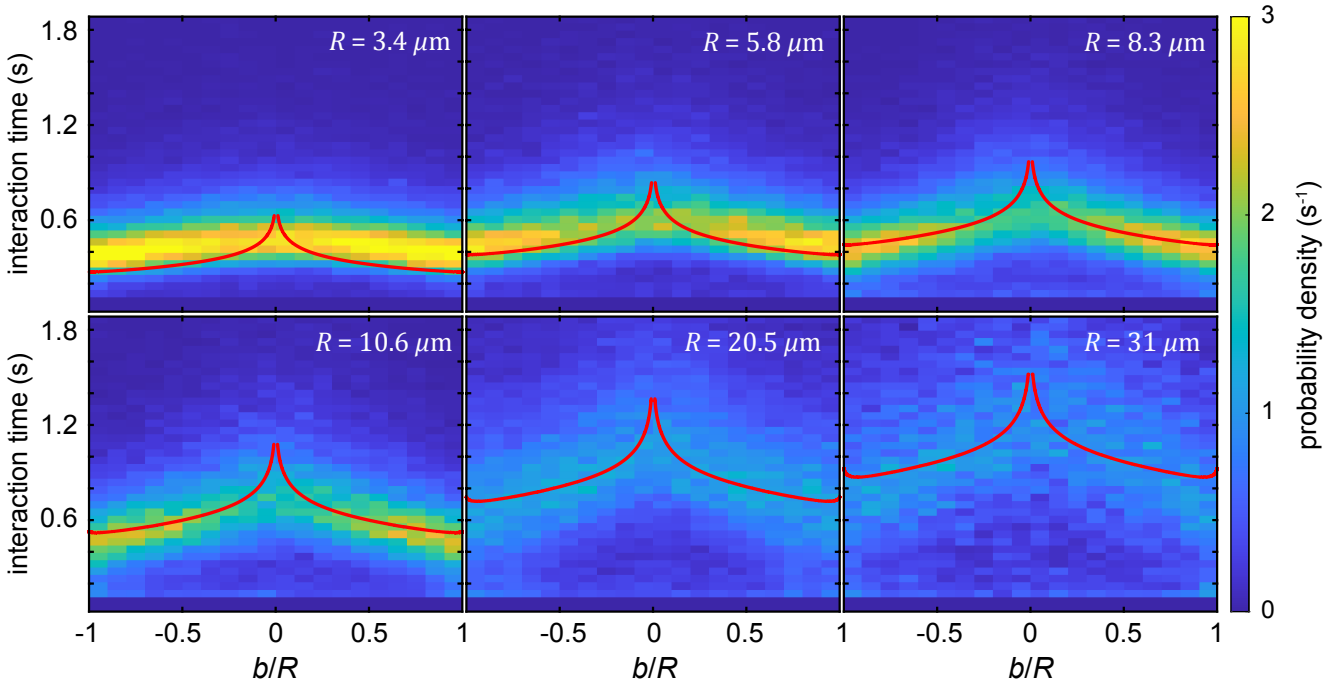

Figure 7: Interaction time distributions as a function of dimensionless impact parameter b/R, across a range of pillar radii. The red lines show the model predictions, which were calculated by adding: (i) the transit time from interaction zone entry to pillar contact using the average cell speed, (ii) the time spent in contact with the pillar using integration of the differential equation, and (iii) the transit time from tangency to exiting the interaction zone using the average cell speed. As $b/R \to 0$ the steric model predicts a divergent interaction time because dynamics of sliding slow as $\alpha_o \to \pi/2$. However, rotational diffusion (and other sources of random rotation) remove the slowest section of the $\alpha(t)$ dynamics and hence the data tend to undershoot the model near $b = 0$. Notably, the 'signal-to-noise' ratio of measured data decreases with increasing pillar radius because the number of pillars and hence number of interactions we can observe in a single field-of-view decreases rapidly with R (see section 6). The spread in interaction times for a fixed bin of b is, at least in part, due to variation in propulsion speed cell-to-cell, which linearly scales the interaction time.

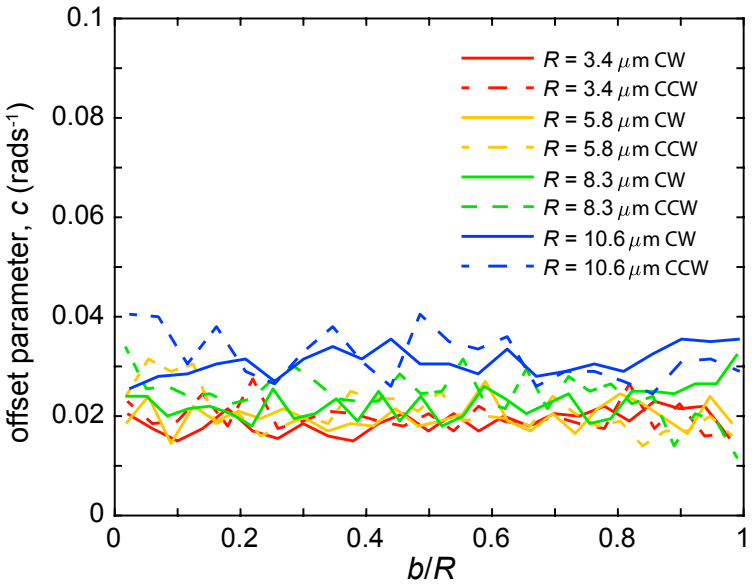

Figure 8: Plot of the von Mises offset parameter (called c above) as a function of b/R across the four smallest radii. The data are the modes from the MLE fits for the parameter estimation. The offsets are roughly constant across $|b/R|$ and approximately chirally symmetric, indicating that the frequency of random scattering events is independent of $|b/R|$ and not related to direction. There is also a rough upward trend in the offset with increasing pillar radius, indicating that random scattering is more common around larger pillars. This may be related to the fact that larger pillars correspond to longer interaction times, and hence a higher probability of a random event (e.g. chemotactic tumble) during the interaction. It may also result from increased hydrodynamic trapping at larger radii, which causes cells to follow trajectories around the pillar for much longer times than steric scattering, but with a random detachment time, and hence random angle.

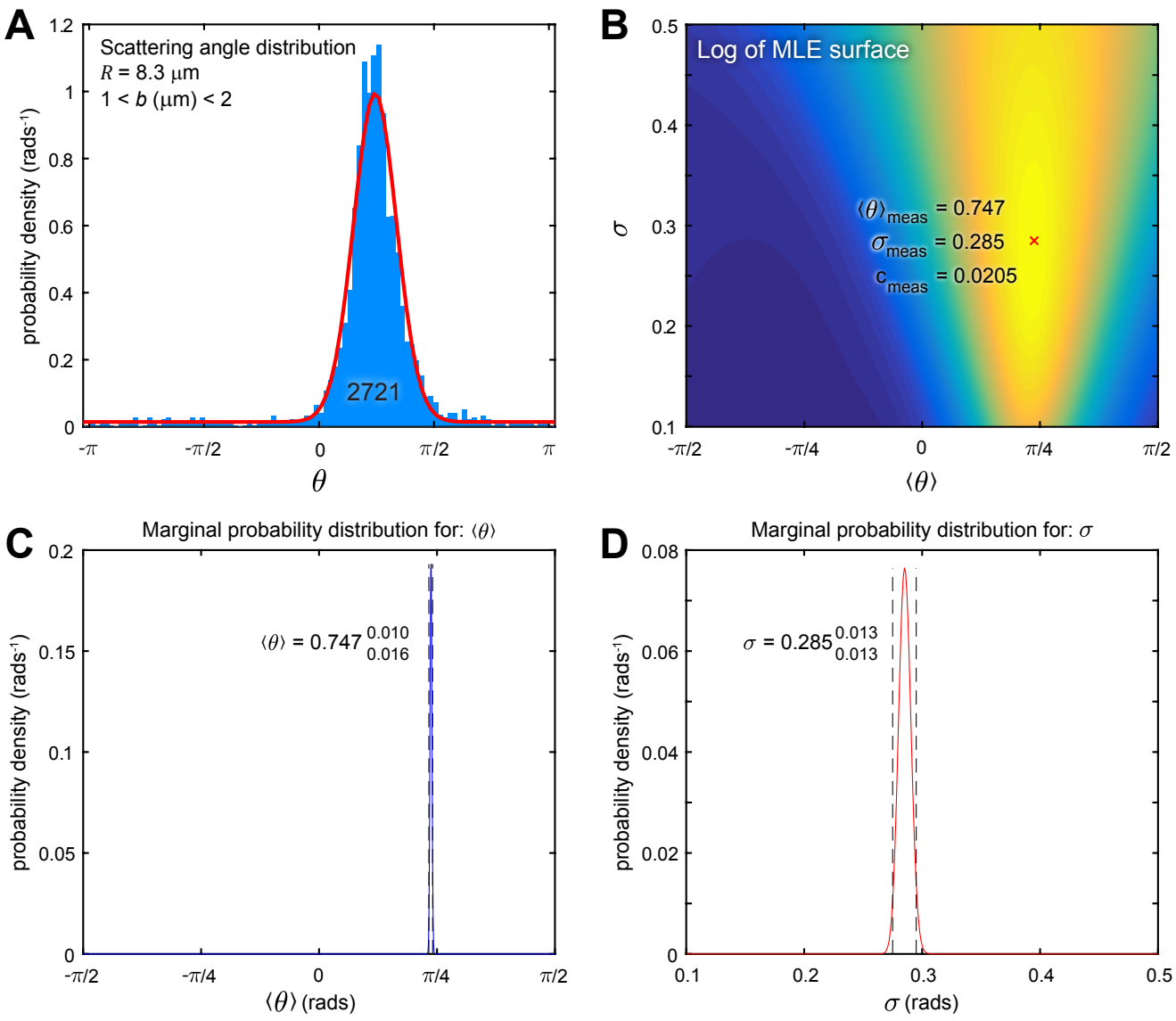

Figure 9: Example output of the MLE fitting. (A) A CW chiral scattering distribution with the MLE fit in red. (B) The natural log of the MLE fit surface for all data in the histogram, showing the mode values for all fit parameters (red 'x'). (C) The probability distribution for the measured value of $\langle\theta\rangle$ showing the mode and 95% confidence interval. (D) The probability distribution for the measured value of σ – the width of the scattering distribution – showing the mode and 95% confidence interval.

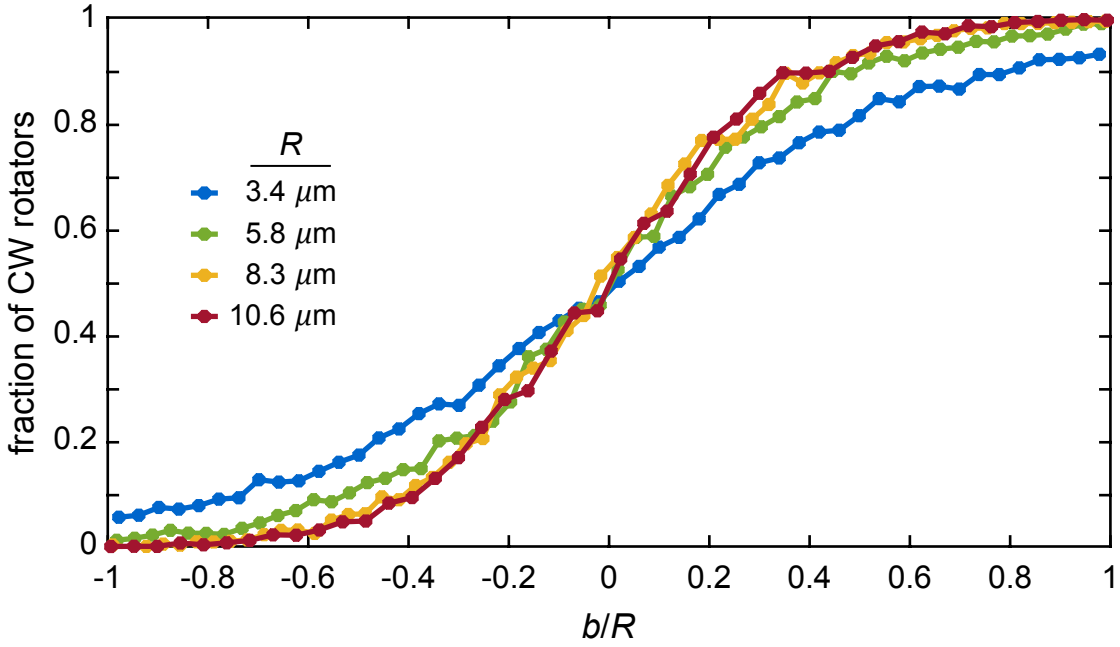

Figure 10: Fraction of cells that rotate clockwise around a pillar as a function of dimensionless impact parameter. Assuming the pillar is centered on a local Cartesian coordinate system, clockwise rotation was defined by cell trajectories that crossed the center-line ($x = 0$) with $y > 0$ in the rotated frame. The naive expectation from the steric model is that this would be an increasing step-function at $b/R = 0$. Based on visual inspection of imaging data, as well as quantitative analysis of breaking the model assumption that the initial contact angle (α_o) is set purely by b and R, we hypothesize that fluctuations in cell orientation upon impact are what produce trajectories that traverse the pillar the 'long way' around (i.e. opposite to the chirality predicted by the steric model). Such fluctuations are caused by translational and rotational diffusion of the cell body, as well as variations in cell morphology that affect initial contact angle. If those fluctuations in orientation due to diffusion and morphology are rotationally isotropic, then we expect (and indeed observe) that these curves are symmetric upon flipping about $b/R = 0$ and $p_{CW} = 1/2$, regardless of pillar radius.

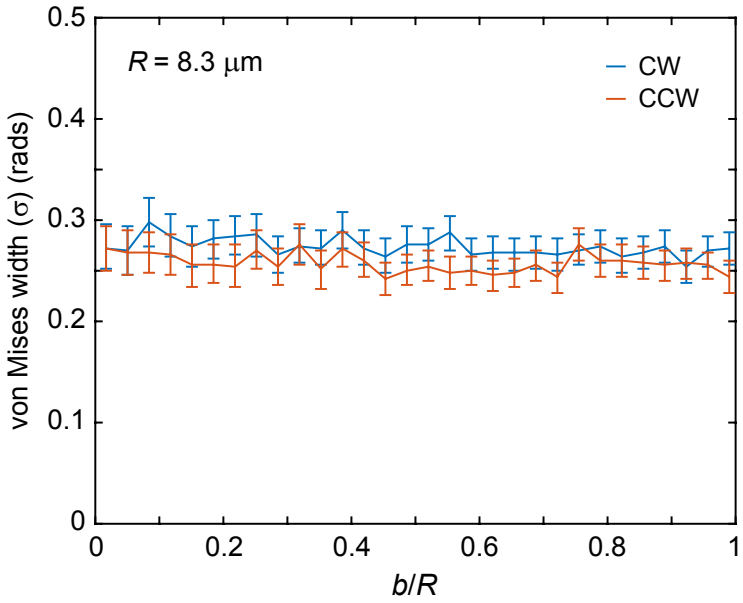

Figure 11: Plot of the von Mises width parameter (called σ above) as a function of b/R for $R = 8.3\,\mu m$. The data are the modes from the MLE fits and the bounds are 95% confidence intervals on the parameter estimation. The width parameter is approximately constant across all values of b/R and is approximately chirally symmetric.

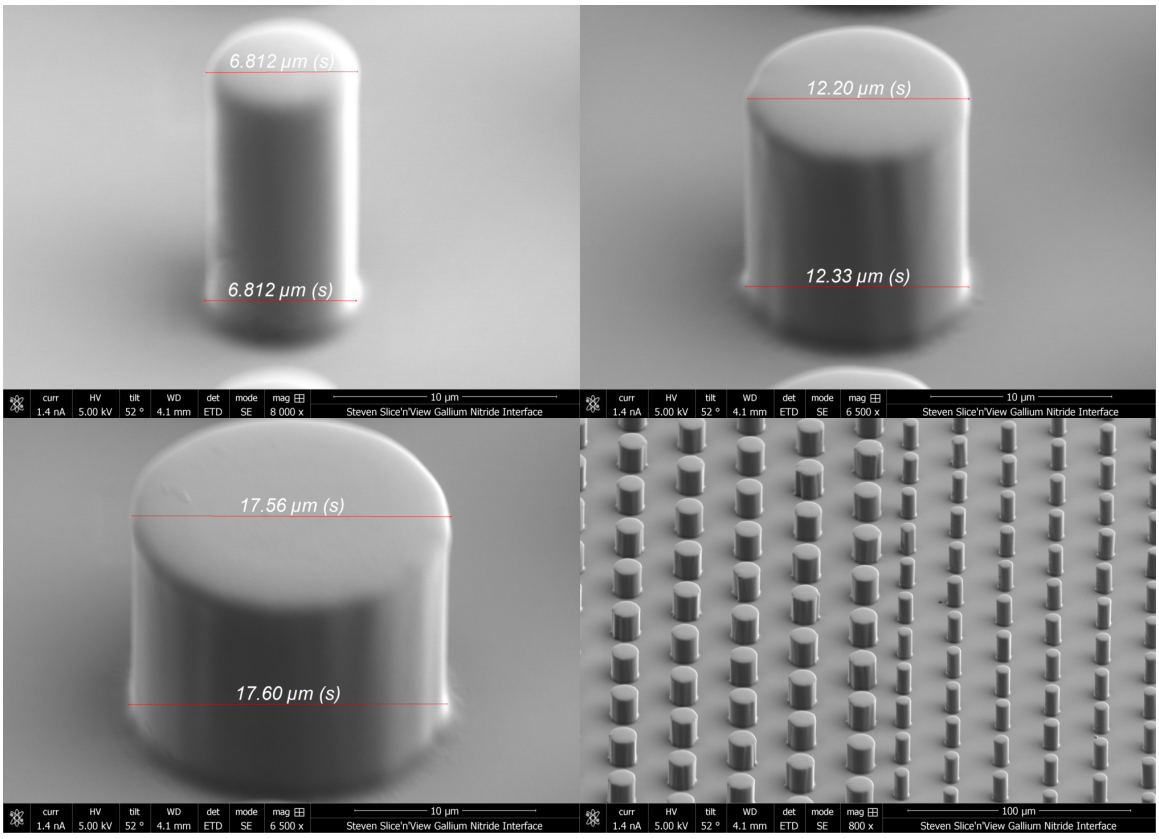

Figure 12: Electron microscopy (EM) images of typical SU-8 polymeric pillars within our microfluidic devices. Pillar radii for each device region were measured using EM imaging.

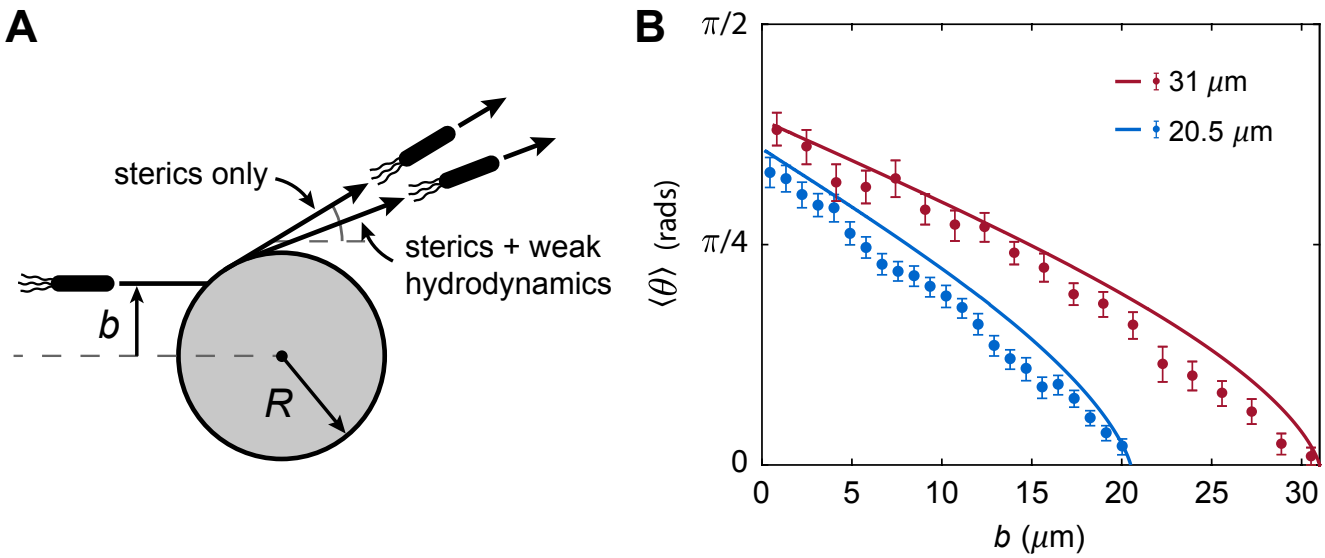

Figure 13: Scattering from larger pillars. (A) Schematic showing the relative scattering angles of a sterics-only scattering event vs. a scattering mechanism that involves hydrodynamic forces that attract the cell to the pillar surface and hence 'over-rotate' it relative to the steric model. (B) Comparison of the model predictions (solid lines) to the measured data for mean scattering angle with 95% confidence intervals around the mean, for the two largest pillars measured. The model overestimates the mean scattering angle at these larger radii, consistent with hydrodynamic forces near these low curvature surfaces over-rotating the cell relative to a sterics-only mechanism, and thus causing a smaller scattering angle.

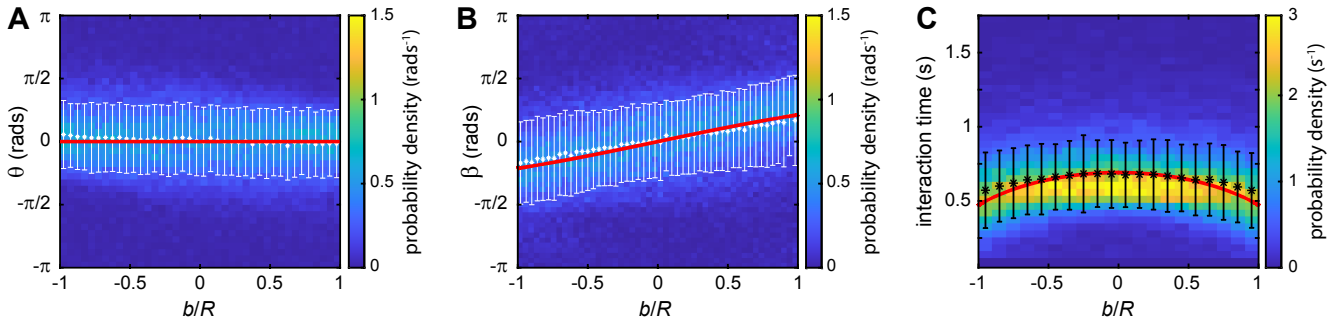

Figure 14: Comparison of data and null-model predictions in the case of no steric interaction. We collected imaging data in a featureless area of our microfluidic device and calculated the same relationships for scattering angle (A, θ), exit angle (B, β), and interaction time (C), assuming a nominal fictitious pillar size of $R = 5.8\,\mu m$ with an interaction zone of $\delta = 2.2\,\mu m$. We used the full data collection and analysis pipeline employed with 'real' steric interaction data to this scenario that lacked steric interactions (call this the 'null model'). The null model makes specific, quantitative predictions of the (mean) relationships between dimensionless impact parameter (b/R) and, respectively, scattering angle (θ), exit angle (β), and interaction time. The heat maps are the measured control data, the red lines are the zero-fit predictions of the null model, again assuming the same $L = 3.75\,\mu m$. The points (white in A and B, black in C) are the means of the measured control data suitable for comparison to the null model. Note that the predictions for $\langle\theta\rangle$ and $\langle\beta\rangle$ under the null model are starkly, qualitatively distinct from the predictions of the steric model. These mean values show a mild systematic deviation from the null model as $|b/R| \to 1$ that lies within a standard deviation of the mean of the data (vertical data bars). We speculate that this results from differences in path length and number-density of paths exiting the interaction zone along its circular boundary. Such deviations break the null-model assumption of persistence length $\lambda \gg (R + \delta)$, producing an asymmetry that progressively grows as $|b/R|$ increases.

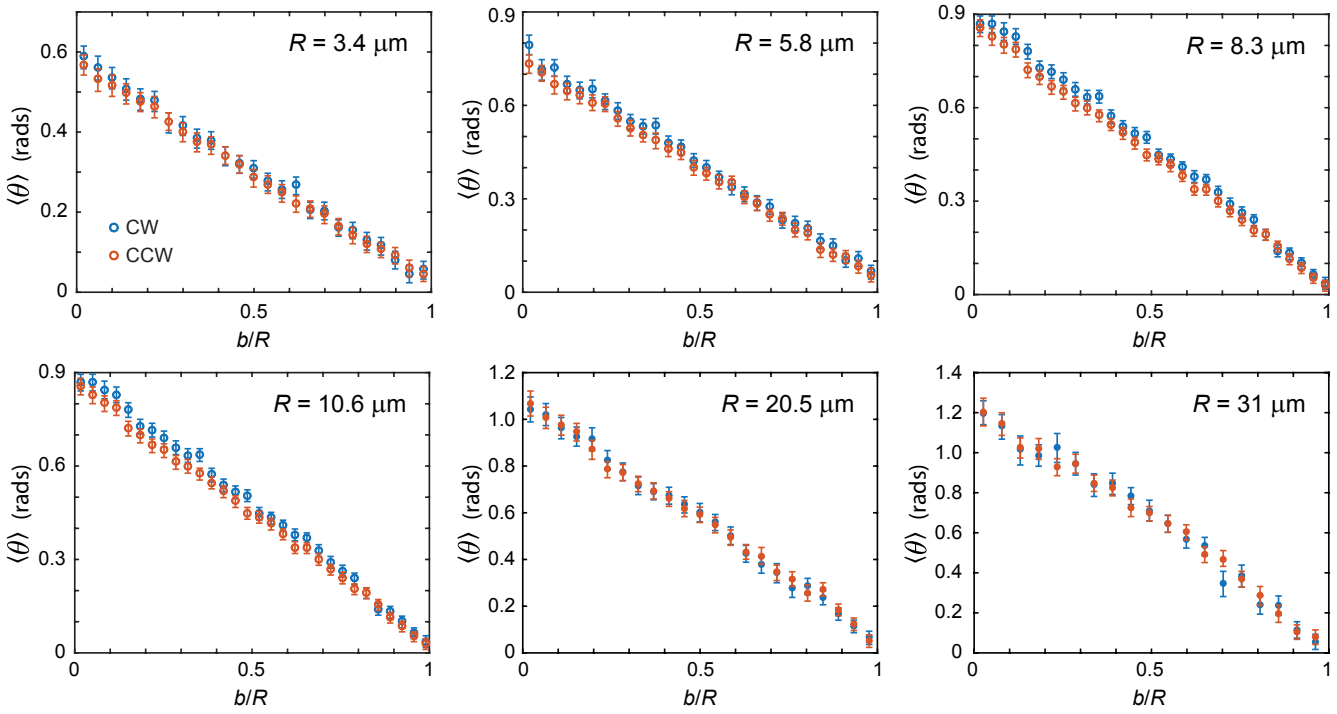

Figure 15: Based on the symmetries present in the propulsion of the bacteria and within the microfluidic device, the distribution of scattering angles as a function of dimensionless impact parameter should be – regardless of mechanism – symmetric when mirrored about both the $\theta = 0$ and $b/R = 0$ axes. Using the MLE fits to a modified von Mises distribution, here we plot $\langle\theta\rangle$ vs. b/R with 95% confidence intervals, with the appropriate mirroring to plot the CW and CCW trajectories overlaid. Across the range of b/R, the data appear approximately symmetric, with mild systematic asymmetry for some radii. These slight chiral asymmetries are likely due to (observed) systematic asymmetries in the radius of the pillars with height due the fabrication process (see Fabrication Details and electron microscopy images, SI Fig. 12).